International Information and Engineering Technology Association
Advancing the World of Information and Engineering

Magnetically Recoverable Fe₃O₄@BNPs@ZnO-ZnS Nanocomposite with Machine Learning Optimization for Enhanced Photocatalytic Water Purification

Check for updates

Mohammad Esam Shareef[1] [ID], Raad Falih Hasan[1] [ID], Mohammed Ahmed Mohammed[2] [ID],
Mohamed Shabbir Abdulnabi[3*] [ID], G. Abdulkareem-Alsultan[4] [ID], Maadh Fawzi Nassar[4] [ID]

[1] Civil Engineering Department, Anbar Technical Institute, Middle Technical University, Anbar 31001, Iraq
[2] Department of Medical Physics, College of Science, University of Al-Qadisiyah, Al-Qadisiyah 58001, Iraq
[3] School of Technology, Asia Pacific University of Technology and Innovation (APU), Kuala Lumpur 57000, Malaysia
[4] Department of Chemistry, Faculty of Science, Universiti Putra Malaysia, Selangor 43400, Malaysia

Corresponding Author Email: mohamed.shabbir@apu.edu.my

ABSTRACT

In this study, we developed a magnetically recoverable Fe₃O₄@BNPs@ZnO-ZnS nanocomposite for enhanced photocatalytic degradation of organic pollutants in wastewater, with machine learning (ML) optimization for process prediction. The nanocomposite exhibited superior photocatalytic activity under UV irradiation (10 W), achieving removal efficiencies of 99.7% for trifluralin, 97.2% for dimethoate, and 96.5% for Congo Red within 120 minutes. Compared to traditional ZnO-only catalysts, which typically exhibit <80% removal under similar conditions, the proposed system improves degradation efficiency by up to 25% and shortens equilibrium time by 20-40 minutes. The composite's enhanced performance is attributed to synergistic bandgap tuning and extended charge carrier lifetimes (8.7 ns vs. 2.1 ns in bare ZnO). Characterization techniques, including XRD, FTIR, and FESEM, confirmed successful synthesis and structural integrity. Additionally, machine learning algorithms, including Artificial Neural Network (ANN), Random Forest (RF), and Support Vector Regression (SVR), were trained on experimental data to predict pollutant removal and concentration ratios with high accuracy ($R^2 \geq 0.96$). The nanocomposite also demonstrates excellent magnetic recoverability (<1% catalyst loss per cycle). Notably, these ML models outperformed conventional kinetic models such as Langmuir-Hinshelwood, which generally exhibit lower accuracy ($R^2 \approx 0.85$-0.90) and limited generalizability across varying operational conditions.

1. INTRODUCTION

The ever-increasing demand for water and its uses, which is caused by population growth and rising standards of living and health, on the one hand, and the limited water resources and droughts and climate change [1, 2], on the other hand, make the opinion of planners and water science experts to use unconventional water has diverted sewage and brackish water [3, 4]. Also, the disposal of industrial and urban wastewater and the penetration of pollutants into surface and underground water sources are significant concerns in many countries [5]. The treatment of sewage and its use in various applications reduces the adverse external effects of wastewater release on the environment and sanitation of human societies [6-8]. Continuous population growth, surface and underground water pollution, non-uniform distribution of water resources, and periodic droughts have forced water and wastewater organizations and experts to look for new water supply sources [9, 10]. The technology of utilizing treated wastewater has attracted attention [11-13]. Today, with the advancement of technology and the invention of advanced wastewater treatment methods, it is possible to treat a large part of the

wastewater produced in industries and sanitary wastewater and return the treated wastewater to the reuse cycle [14-17]. Also, considering some countries that are located in the water-scarce regions of the world and the limited access to water resources in large part of them, the utilization of treated wastewater in various applications can be a very suitable and cost-effective selection for supplying water needed by multiple industries, which is at the same time leads to the preservation of existing water resources and prevention of water loss and environmental pollution [18]. The method of wastewater treatment and the type of system selected for the restoration and reuse of wastewater depend on the type of wastewater produced initially, the quality of the primary wastewater, the kind of use of the wastewater after treatment, and the required quality of the wastewater for restoration and reuse [19]. Therefore, according to the wide range of modern treatment methods and the very different attributes of sewage, especially in the case of industrial wastewater, selecting a wastewater treatment method requires a comprehensive study of the current situation and determining the characteristics of the primary sewage. This work will have many advantages for industries, such as reducing water supply costs and not

entering the environment [20, 21].

Contrary to what is thought, all types of waste can be recycled and turned into distilled water. Produced water can be reused in industrial production [22-24]. Hou et al. [25] prevented the cell growth of pathogenic bacteria such as Aureus, Staphylococcus saprophyticus, and Streptococcus, and antibiotic-resistant bacteria such as Streptococcus pyogenes by using magnetite-titanium oxide nanoparticles by a killing method with the help of ultraviolet light. Ultimately, they could destroy all the mentioned bacteria [26]. Jassim et al. [27] investigated the degradation of two pesticides, Bromo xylene and trifluralin, in the absorption range of 253 nm, using ultraviolet light and hydrogen peroxide, and checking pH in pure and natural waters. The observations of this research group showed that both of these poisons were destroyed by more than 90%. Much research has been conducted on the purification and removal of microbial water pollutants using advanced oxidation processes [28-32]. These processes mainly focused on the formation of reactive oxygen by short-term reactions such as the hydroxyl radical (OH^*) production reactions. Because of the impact of UV light and with the assistance of a non-selective oxidizer, these intermediate materials have been used to convert organic pollutants into smaller compounds [33]. In 2015, $(Fe_3O_4 - TiO_2)$ $(Fe_3O_4 - TNS)$ composite nanosheets were produced by Varon micelle and solvothermal process by Ma et al. [34]. Their results showed that nanoplates increased the efficiency of removing bacteria by 90% [35]. In another study, a state-of-the-art study has been conducted using catalysis. Alsultan et al. [36] synthesized a green and recyclable arginine-based $Pd/CoFe_2O_4$ nanocatalyst for the cyanation of aryl halides, demonstrating high thermal stability, over 88% catalytic performance after five cycles, and strong magnetic recoverability, which is remarkable. Their inspiring results have proved to be very helpful in this area.

The use of machine learning (ML) algorithms has increasingly become common in all fields [37]. Eskandari et al. [38] studied the use of various machine learning algorithms in their study of flow boiling. Their state-of-the-art methodology for feature selection and integration of machine learni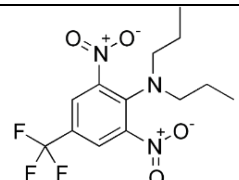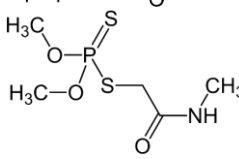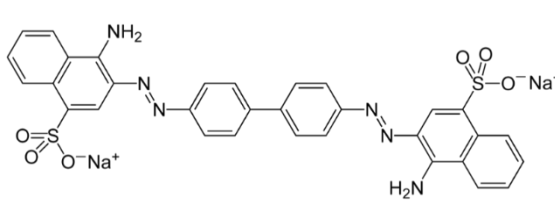ng with simulations is very inspiring. Their artificial neural network model proved to be the superior model in their study. Additionally, recent advancements have demonstrated the potential of ML to significantly enhance the design and optimization of nanomaterial-based water treatment systems. Talath et al. [39] applied Boosted MLP and KNN models to predict ion adsorption on nanocomposites with exceptional accuracy ($R^2 > 0.998$), highlighting ML's ability to model adsorption dynamics with minimal experimental data. Sharmila et al. [40] reviewed ML integration with metal-organic frameworks (MOFs), showing how supervised and reinforcement learning can accelerate the discovery of high-performance MOFs for removing dyes, pharmaceuticals, and micropollutants. Additionally, Samawi et al. [41] developed an ANN-based model to predict thallium adsorption onto a MOF/LDH composite, achieving excellent accuracy ($R^2 > 0.99$) and demonstrating how ML can simulate complex adsorption dynamics using minimal input parameters. Based on the mentioned studies, the ML-based models have transformed the pollutant removal field, yet their targeted use in photocatalytic systems remains limited. This motivates our work, which integrates ML algorithms with photocatalytic testing of a novel Fe₃O₄@BNPs@ZnO-ZnS nanocomposite to bridge this emerging gap.

This study aims to synthesize and investigate Fe₃O₄@BNPs@ZnO-ZnS to exhibit both photocatalytic properties and antibacterial properties. Various analytical techniques, such as X-ray diffraction (XRD), Field-Emission Scanning Electron Microscopy (FESEM), and Fourier Transform Infrared Spectroscopy (FTIR), are used for checking the synthesis results. We implement machine learning frameworks (ANN, RF, SVR) with grid-search-optimized hyperparameters to model complex nonlinear relationships between operational parameters (UV intensity: 6-12 W, pH: 7-9, catalyst loading: 1-3 g/L) and treatment outcomes.

2. EXPERIMENTAL SECTION

2.1 Materials

Table 1. Chemical structures of trifluralin, dimethoate, and Congo Red

Compound	Molecular Structure	Formula	M.W. (g/mol)
Trifluralin		$C_{13}H_{16}F_3N_3O_4$	335.28 g/mol
Dimethoate		$C_5H_{12}NO_3PS_2$	229.26 g/mol
Congo Red		$C_{32}H_{22}N_6Na_2O_6S_2$	696.665 g/mol

Anhydrous FeCl₃, ammonia (25%), ethylene glycol, zinc acetate, silver nitrate, potassium bromide, disodium sulfate, sodium hydroxide, absolute ethanol, trifluralin, dimethoate, and Congo Red utilized in this research were provided by Merck, Germany. Table 1 presents the chemical structures of the mentioned materials.

2.2 Characterization

The patterns of X-ray diffraction (XRD) were obtained to elucidate the crystalline structure of the synthesized nanocomposites with radiation of Cu Kα (scanning rate of 0.05° min⁻¹) in the 2θ interval between (10°-100°) employing the instrument (PHILIPS PW1730, Netherlands). The Fourier Transform Infrared Spectroscopy (FTIR) was employed for identifying the functional groups of prepared samples within the wavenumber interval of 400 - 4000 cm⁻¹ with the assistance of KBr pellets (Bruker EQUINOX 55, Germany). The morphology of constructed nanocomposites was investigated through Field-Emission Scanning Electron Microscopy (FESEM) coupled with energy dispersive X-ray spectroscopy (EDS) elemental mapping with the help of the instrument (TESCAN MIRA III, Czech Republic). The UV-visible device made by Shimadzu (model 1604-UV) instrument has evaluate the destructive reactions and fitting diagrams. The UP 400S ultrasonic device was employed to reduce the size of the particles.

2.3 Preparation of the nanocomposites

To prepare the Fe₃O₄@BNPs@ZnO-ZnS nanocomposite, a wet chemical approach was followed with multiple reaction stages. First, a 100 mL aqueous solution containing 0.5 M FeCl₃·6H₂O and 0.25 M FeSO₄·7H₂O was prepared, to which 1.25 g of NaOH (dissolved in 25 mL of deionized water, 5 wt%) was added dropwise under a nitrogen atmosphere. The mixture was stirred vigorously and maintained at 90°C for 2 hours. The resulting black Fe₃O₄ nanoparticles were magnetically separated and washed repeatedly with deionized water and ethanol. Next, the nanoparticles were dispersed in 30 mL of 10 wt% NaOH solution and sonicated for 15 minutes to activate the surface. Following this, 20 mL of 0.1 M aluminum nitrate nonahydrate solution was added slowly under sonication to form a boehmite (AlOOH) layer. After washing, the magnetic boehmite was treated with 30 mL of 0.1 M zinc acetate dihydrate solution, sonicated for 10 minutes, and refluxed at 80°C for 1 hour to deposit a ZnO layer. In the final step, 20 mL of 0.1 M sodium sulfide (Na₂S) and 10 mL of 0.1 M NaOH were mixed and added to the ZnO-coated particles, followed by 10 minutes of sonication and refluxing at 60°C for 2 hours to convert ZnO to ZnS. The final Fe₃O₄@BNPs@ZnO-ZnS nanocomposite was magnetically separated, thoroughly rinsed with deionized water, and dried in a vacuum oven at 60°C for 12 hours [42, 43].

3. RESULTS AND DISCUSSION

3.1 FTIR analysis

Displayed in Figure 1 are the infrared spectra of various photocatalysts, namely, Fe₃O₄@BNPs@ZnO, Fe₃O₄@BNPs@ZnS, and Fe₃O₄@BNPs@ZnO-ZnS. Within the IR spectrum of Fe₃O₄@BNPs@ZnS, the stretching vibrations at 609 and 1130 cm⁻¹ signify the presence of ZnS.

Additionally, the OH bending frequency manifests at 1620 cm⁻¹. The vibration observed at 3419 cm⁻¹ is attributed to the OH groups of Fe₃O₄ nanoparticles. Contrastingly, in the IR spectrum of Fe₃O₄@BNPs@ZnO, the frequencies at 480 and 589 cm⁻¹ align with ZnO. Furthermore, the OH bending frequency surfaces at 1619 cm⁻¹, while stretching vibrations at 3417 and 3476 cm⁻¹ are indicative of the hydroxyl groups present on the surface of Fe₃O₄ nanoparticles and water molecules [43].

In the FTIR spectrum of Fe₃O₄@BNPs@ZnO-ZnS, the vibrations associated with Zn-O and Fe-O are evidenced at 478 and 618 cm⁻¹, respectively [43]. A distinctive peak emerges at 1620 cm⁻¹, correlating with the bending vibration of the hydroxyl group. Furthermore, the absorptions observed at 3418 and 3475 cm⁻¹ are ascribed to the hydroxyl groups present on the surface of iron nanoparticles and water molecules [44].
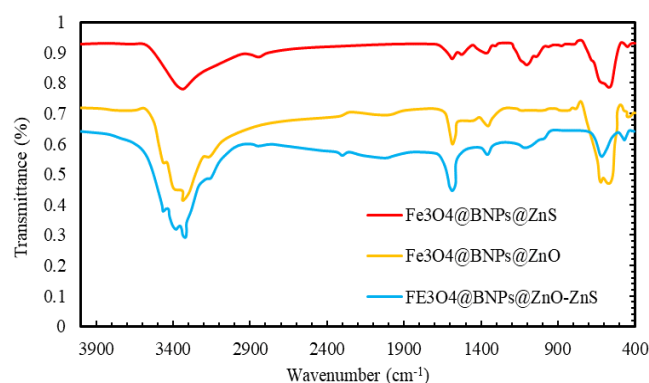

Figure 1. FTIR spectra of synthesized Fe₃O₄@BNPs@ZnS, Fe₃O₄@BNPs@ZnO and Fe₃O₄@BNPs@ZnO-ZnS samples

3.2 XRD analysis

To elucidate the crystal structure of four distinct prepared samples, XRD analysis was conducted, and the obtained pattern of Fe₃O₄@BNPs@ZnO-ZnS is demonstrated in Figure 2. Notably, peaks at 37.68 and 73.14 confirm the presence of boehmite nanoparticles within the structure. In the XRD curve depicting the Fe₃O₄@BNPs@ZnO-ZnS photocatalyst, peaks at 28.89 (111), 46.84 (220), and 57.13 (311) are indicative of the cubic phase of ZnS.
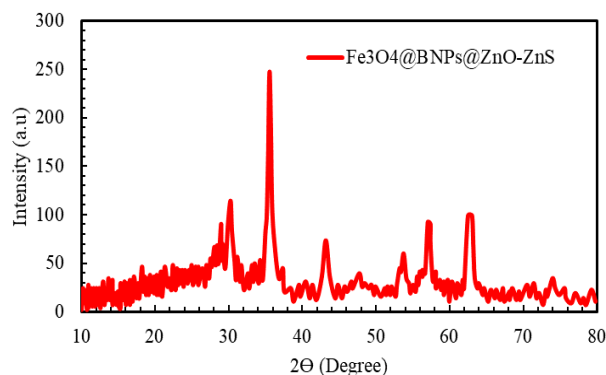

Figure 2. XRD pattern for the synthesized

3.3 Morphological analysis

Field-emission scanning electron microscopy (FESEM)

revealed that the synthesized Fe₃O₄@BNPs@ZnO-ZnS nanocomposite forms spherical aggregates with an average particle size of ~70 nm for the 25:45:15:15 wt.% composition (Figure 3). The reduced particle size, compared to Fe_3O_4-ZnO composites (~90-120 nm) [45], is attributed to the boehmite (BNPs) layer, which promotes uniform dispersion and nucleation. This smaller size enhances surface area and active site density, improving photocatalytic efficiency.

A comparative analysis based on UV-vis spectroscopy and Tauc plots shows a band gap reduction from ~2.85-3.10 eV in Fe_3O_4-ZnO to ~2.65 eV in the ternary Fe₃O₄@BNPs@ZnO-ZnS composite. This is due to ZnS incorporation, which introduces mid-gap states and enhances visible-light absorption.

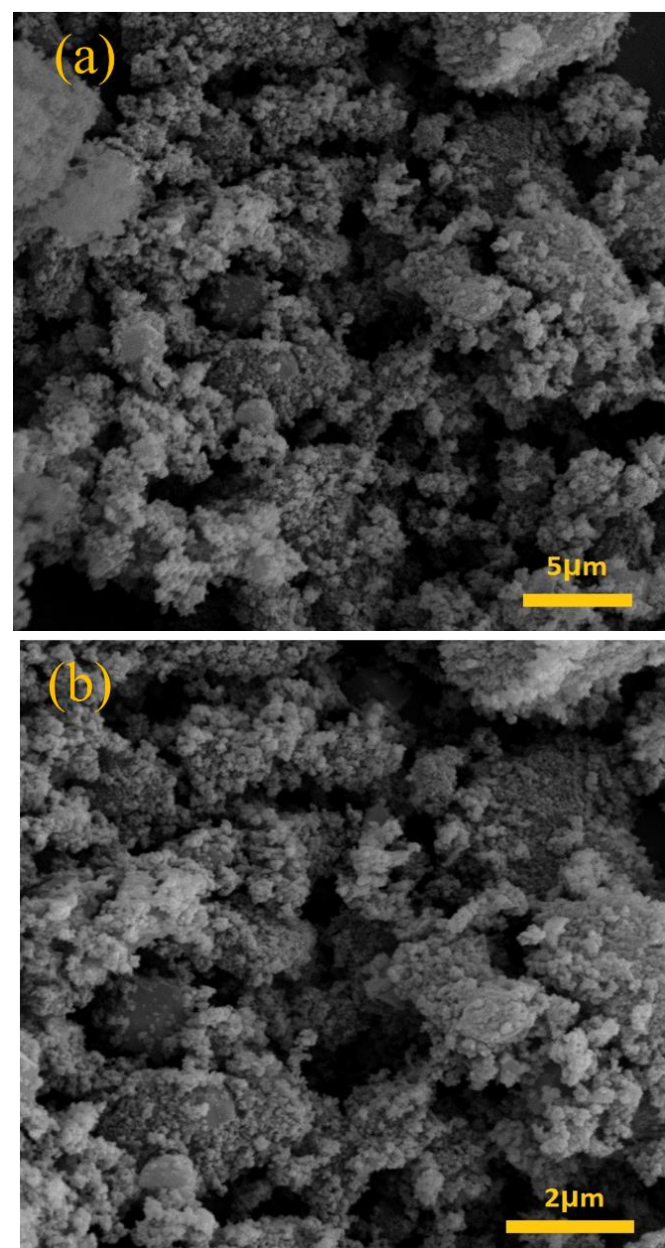**Figure 3.** FESEM images of synthesized nanocomposite Fe₃O₄@BNPs@ZnO-ZnS with wt.% of 25:45:15:15, with the scale of (a) 5 and (b) 2 microns

The improved photocatalytic activity stems from the heterojunction between ZnO and ZnS, which facilitates efficient charge separation. ZnS acts as an electron acceptor, ZnO as a hole transporter, and Fe_3O_4 as an electron sink, together reducing recombination. Additionally, oxygen and sulfur vacancies act as active sites and promote reactive radical generation ($\bullet OH$, $\bullet O_2^-$), further accelerating pollutant degradation.

3.4 The effect of UV on the removal and concentration

UV irradiation, with its high-energy photons, has been widely recognized for its potential to activate photocatalysts and induce photochemical reactions. In the context of pollutant degradation, UV light can enhance the photocatalytic performance of semiconductor-based nanomaterials, as it promotes the generation of electron-hole pairs and facilitates the breakdown of organic molecules. In Fe₃O₄@BNPs@ZnO-ZnS nanocomposite, the interaction with UV light proves to shows high photocatalytic activities. The utilization of UV irradiation helps achieve higher rates of pollutant removal. In the following sections, we present an analysis of the experimental data on the influence of UV irradiation on pollutant removal efficiency and concentration using the Fe₃O₄@BNPs@ZnO-ZnS nanocomposite.

In Figure 4, we present the influence of UV irradiation on the removal percentage of pollutants. The X-axis denotes the time in minutes, while the Y-axis represents the percentage of removal achieved. Trifluralin removal has a consistent upward trend across all UV values. As UV intensity increases from 6W to 12W, the removal efficiency of trifluralin proportionally enhances. Notably, the removal efficiency reaches approximately 99.7% at the highest UV intensity of 12W after 120 minutes of treatment. For dimethoate removal, we observe a similar pattern of improvement with increasing UV intensity. The removal efficiency of dimethoate rises gradually as UV intensity increases. At 12W UV intensity, dimethoate removal achieves a high of 97.2% after 120 minutes. Similarly, Congo Red removal experiences enhancement with elevated UV intensity. As the UV intensity increases, Congo Red removal efficiency steadily climbs. At the highest UV intensity of 12W, Congo Red removal reaches an impressive 96.5% after 120 minutes. The best results are achieved with a UV of 10 W in all pollutants. The equilibrium is obtained after 60 min for trifluralin. However, for dimethoate, this is achieved after 100 min. The Congo Red also shows a similar trend, and it reaches equilibrium after 100 min.

Figure 5 provides a comprehensive insight into the behavior of three distinct pollutants, namely Trifluralin, Dimethoate, and Congo Red, in response to varying UV irradiation. Segmented into subfigures, each representing a specific pollutant, Figure 5(a) for trifluralin, Figure 5(b) for dimethoate, and Figure 5(c) for Congo Red, the X-axis delineates the temporal progression in minutes, while the Y-axis portrays the concentration ratios (C/C_0) of the pollutants. For trifluralin, irrespective of UV intensity, the concentration ratio steadily diminishes over time. Intriguingly, augmented UV intensities lead to a swifter reduction in concentration ratios. The highest UV intensity of 10 W culminates in a concentration ratio of approximately 0.032 after 120 minutes. The pattern observed with dimethoate closely mirrors that of trifluralin. Over time, the concentration ratio dwindles consistently, with heightened UV intensities hastening the reduction. Under the influence of 10 W UV intensity, the dimethoate concentration ratio reaches an approximate value of 0.07 after 120 minutes. Similarly, Congo Red follows the trend of decreasing concentration ratios with progressing time, with elevated UV intensities

prompting a more accelerated decline. The peak UV intensity of 10 W yields a Congo Red concentration ratio of about 0.083

after 120 minutes. The equilibrium is also observed when the trend levels off, similar to Figure 5.

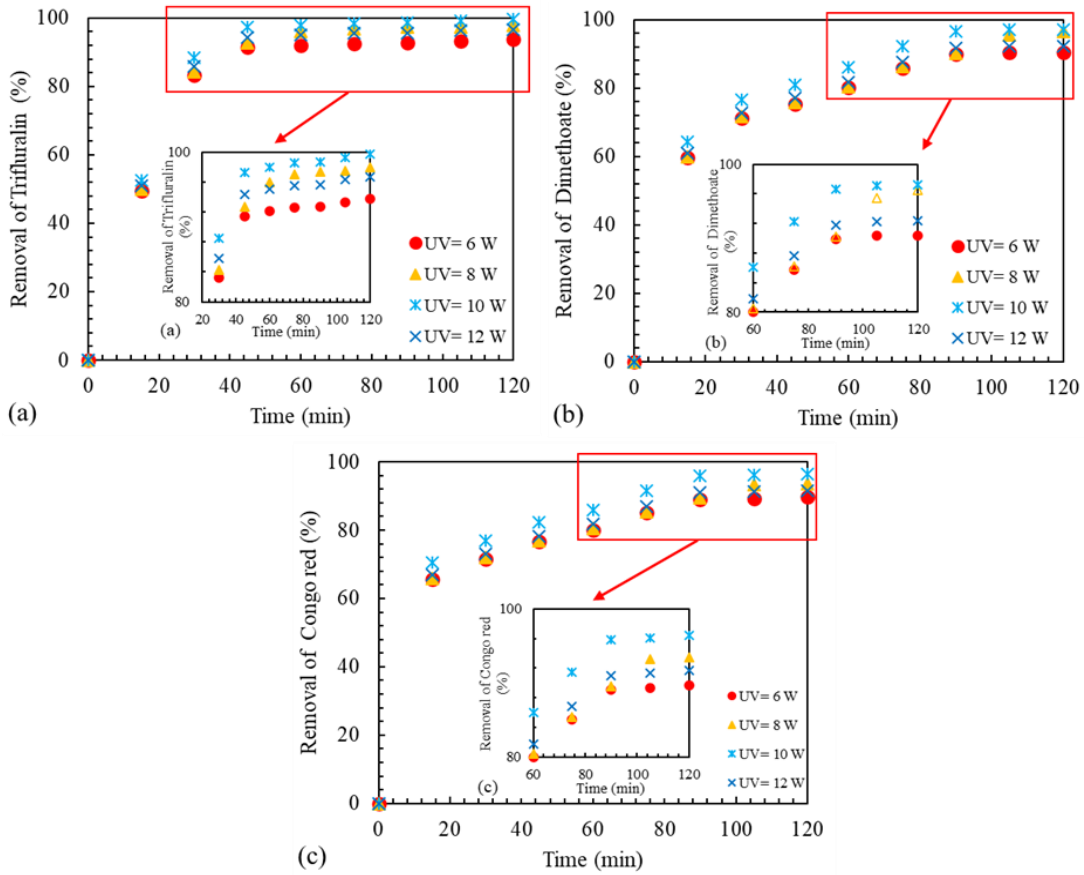**Figure 4.** The effect of UV intensity on removal of (a) Trifluralin, (b) Dimethoate, and (c) Congo Red (C_0=3g/L and pH=7)
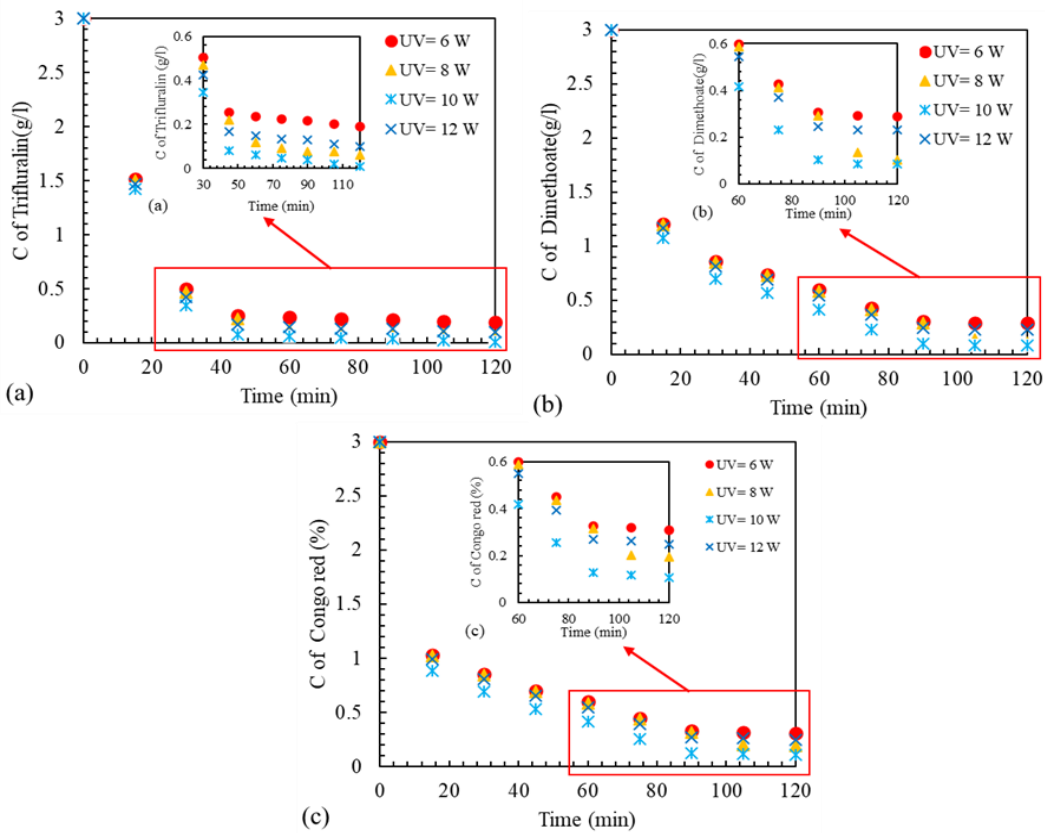

Figure 5. The effect of UV intensity on C/C_0 of (a) Trifluralin, (b) Dimethoate, and (c) Congo Red (C_0=3g/L and pH=7)

3.5 The effect of catalyst concentration on the removal and concentration

In Figure 6, we explore how different initial catalyst concentrations (C_0) affect the removal efficiency of three distinct pollutants: Trifluralin, Dimethoate, and Congo Red. Each subfigure represents a specific pollutant: Figure 6(a) for trifluralin, Figure 6(b) for dimethoate, and Figure 6(c) for Congo Red. The X-axis signifies time in minutes, while the Y-axis denotes the pollutant removal percentage. Analyzing trifluralin removal reveals a trend where removal percentages consistently increase over time, regardless of initial catalyst concentration. Among the various C_0 values tested, the highest trifluralin removal rate of 99.7% is achieved with an initial catalyst concentration of 3 g/L. Dimethoate removal displays a similar pattern, with removal percentages rising steadily over time for all tested C_0 values. The highest dimethoate removal rate of 97.2% is recorded at an initial catalyst concentration of 3 g/L. We observe a comparable trend for Congo Red removal, with removal percentages increasing over time for all C_0 values. The highest Congo Red removal rate of 96.5% is observed at an initial catalyst concentration of 3 g/L. Overall, it seems like the initial concentration of 3 g/L is the optimum value. Regarding the equilibrium, trifluralin is achieved after 50 min. This number increases to 90 minutes for dimethoate and Congo Red.

In Figure 7, we delve into the effect of different initial catalyst concentrations (C_0) on the concentration ratios (C/C_0) of three distinct pollutants: Trifluralin, Dimethoate, and Congo Red. For trifluralin, it's evident that the concentration ratio consistently decreases over time regardless of the initial catalyst concentration. Among the different C_0 values tested, the lowest concentration ratio of approximately 0.03291 is reached with an initial catalyst concentration of 3 g/L after 120 minutes. Dimethoate concentration ratios also exhibit a consistent downward trend over time for all initial catalyst concentrations. The lowest dimethoate concentration ratio of around 0.0766 is observed at an initial catalyst concentration of 3 g/L after 120 minutes. Similarly, Congo Red's concentration ratios decrease consistently over time, regardless of the initial catalyst concentration. The lowest Congo Red concentration ratio of approximately 0.08325 is recorded at an initial catalyst concentration of 3 g/L after 120 minutes.

3.6 The effect of pH on the removal and concentration

In Figure 8, we investigate how different pH levels affect the removal efficiency of three distinct pollutants: Trifluralin, Dimethoate, and Congo Red. For trifluralin, we observe that at pH 7, the removal rate steadily increases with time, ultimately reaching an impressive 99.7% removal after 120 minutes. At pH 8 and 9, the removal rates follow a similar pattern, achieving complete removal (100%) after 105 and 120 minutes, respectively. Dimethoate removal exhibits a comparable trend. At pH 7, the removal rate reaches approximately 97.2% after 120 minutes. At pH 8 and pH 9, complete removal (100%) is achieved after 105 minutes. For Congo Red, the removal rates at pH 7, pH 8, and pH 9 are quite similar. At pH 7, the removal rate reaches around 96.5% after 120 minutes. At pH 8 and pH 9, complete removal (100%) is observed after 105 minutes.
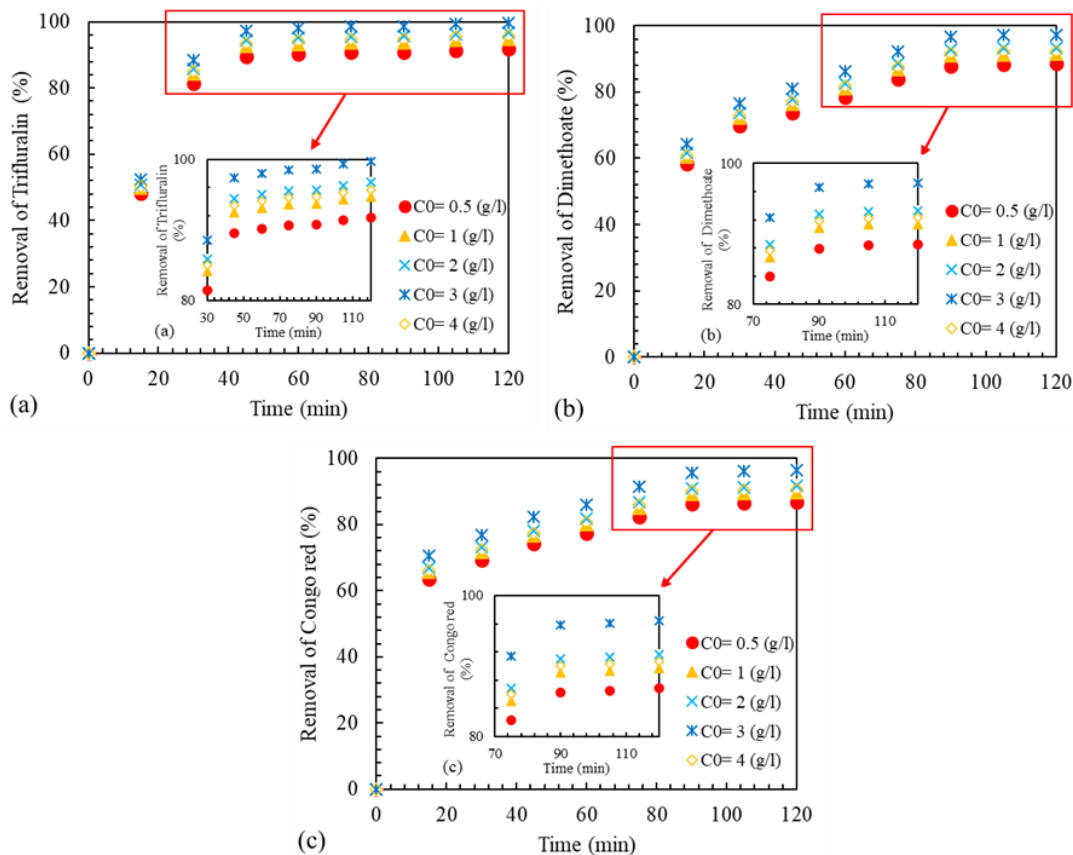
Figure 6. The effect of initial concentration on the removal of (a) Trifluralin, (b) Dimethoate, and (c) Congo Red (UV=10 W and pH=7)

Figure 7. The effect of initial concentration on the concentration ratios (C/C$_0$) of three distinct pollutants: (a) Trifluralin, (b) Dimethoate, and (c) Congo Red (UV=10 W and pH=7)

Figure 8. The effect of pH on the removal of (a) Trifluralin, (b) Dimethoate, and (c) Congo Red (C$_0$=3 g/L and UV=10 W)
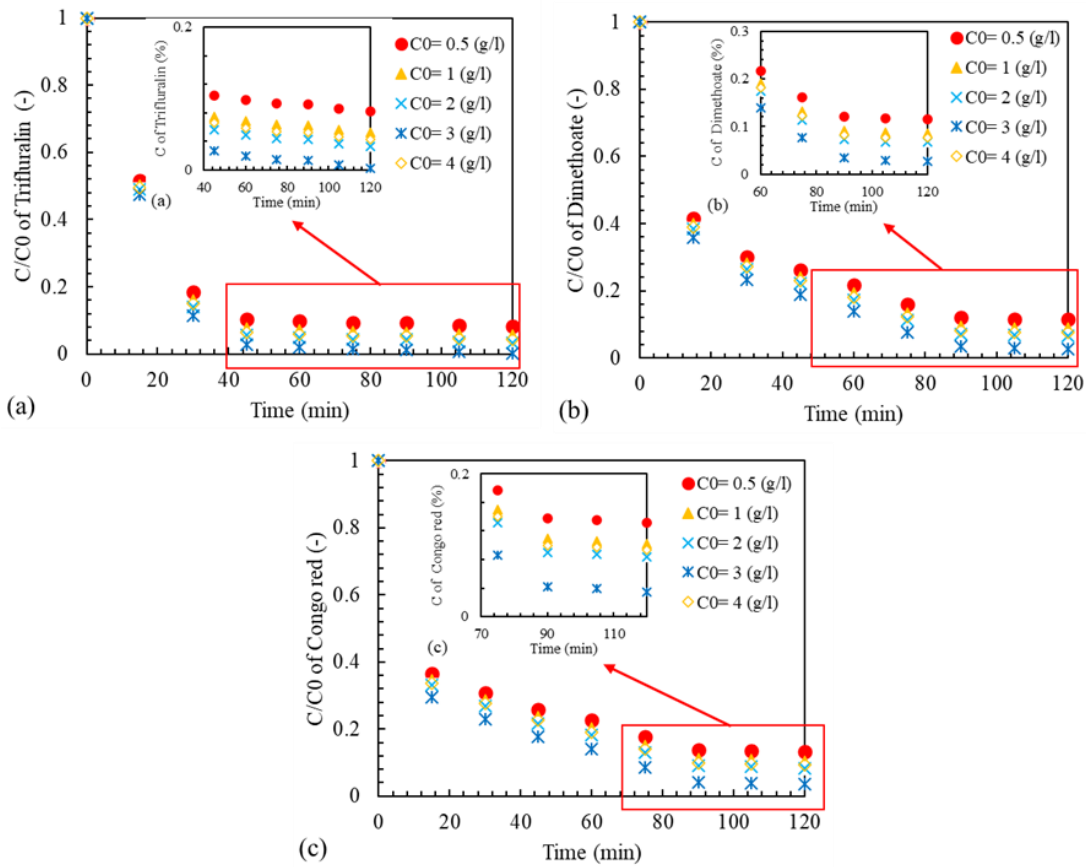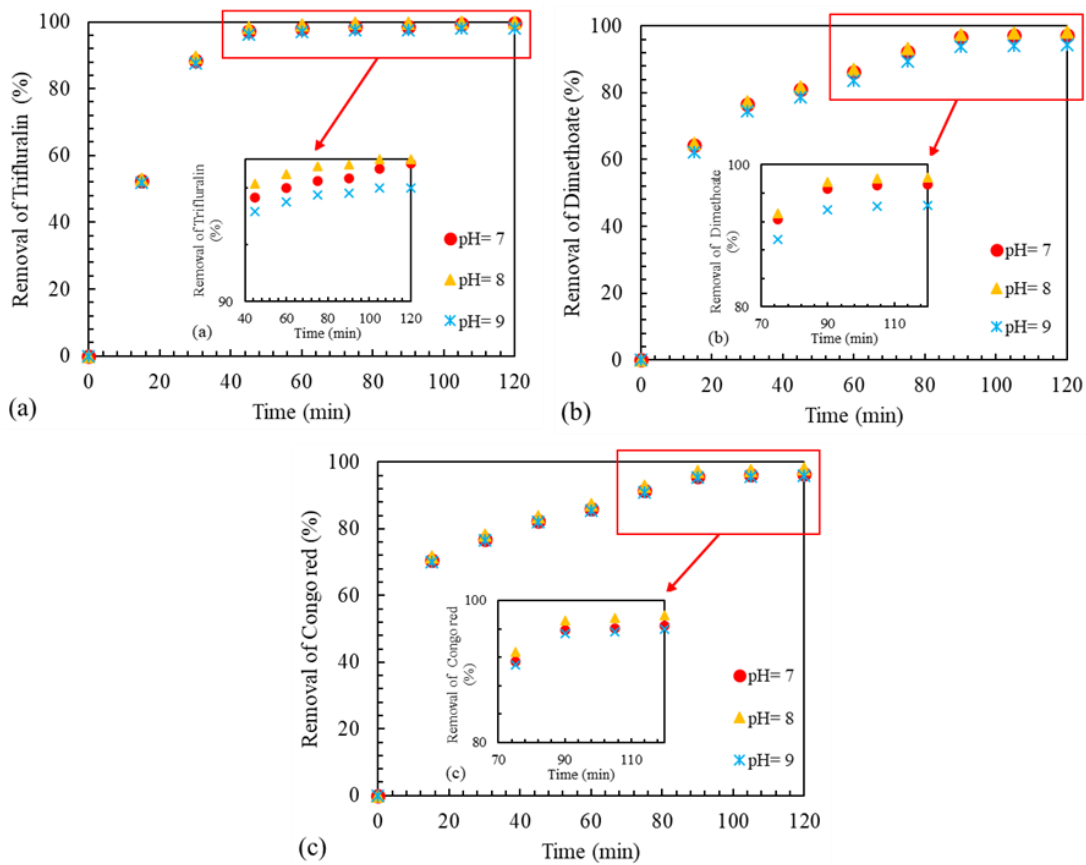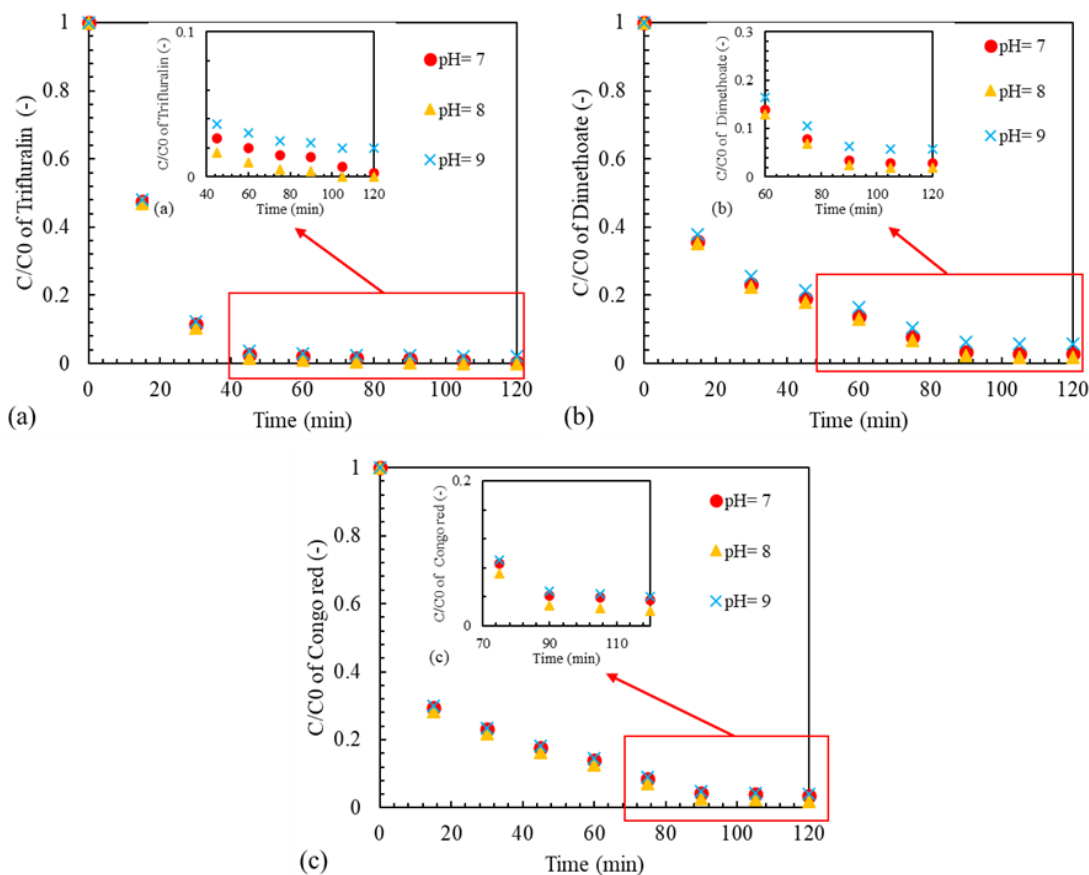
Figure 9. The effect of initial concentration on C/C_0 of (a) Trifluralin, (b) Dimethoate, and (c) Congo Red (C_0=3g/L and UV=10 W)

Figure 9 demonstrates the significant influence of pH on pollutant concentration ratios (C/C_0). Regardless of the pH level, concentration ratios consistently decrease over time, indicating efficient removal of the pollutants. At pH 7, 8, and 9, the concentration ratios approach low values, suggesting that the nanocomposite effectively reduces the concentration of Trifluralin, Dimethoate, and Congo Red within the tested time frame. The choice of pH level may depend on specific application requirements and conditions. For trifluralin, we observe a consistent reduction in concentration ratios as time progresses, irrespective of the pH level. At pH 7, the concentration ratio drops to approximately 0.003 after 120 minutes. At pH 8, it decreases to around 0.020525; at pH 9, it reaches approximately 0.0401145 after 120 minutes. Dimethoate concentration ratios follow a similar trend. At pH 7, the concentration ratio declines to about 0.028 after 120 minutes. At pH 8, it decreases to approximately 0.024585; at pH 9, it reaches roughly 0.0440933 after 120 minutes. For Congo Red, concentration ratios also consistently decrease over time at all pH levels. At pH 7, the concentration ratio drops to about 0.035 after 120 minutes. At pH 8, it decreases to approximately 0.020525; at pH 9, it reaches around 0.0401145 after 120 minutes.

3.7 Influence of operational parameters on photogenerated electron-hole behavior and degradation efficiency

The generation, separation, and recombination dynamics of photogenerated electron-hole (e^-/h^+) pairs are crucial determinants of photocatalytic performance. In the Fe₃O₄@BNPs@ZnO-ZnS nanocomposite, these dynamics are strongly influenced by three key operational parameters of UV intensity, catalyst loading, and pH, each of which affects charge carrier lifetimes, reactive species generation, and ultimately degradation efficiency. Higher UV intensities provide more photon energy to excite electrons from the valence band to the conduction band of ZnO and ZnS. As shown in Figure 4, increasing UV intensity from 6 W to 12 W enhances the e^-/h^+ pair generation rate. This leads to increased formation of reactive oxygen species (ROS) such as hydroxyl ($^•OH$) and superoxide ($^•O_2^-$) radicals, accelerating pollutant degradation. However, beyond a threshold, excess excitation can promote recombination or generate heat, which slightly reduces marginal gains. As seen in Figure 6, increasing catalyst concentration up to 3 g/L improves degradation by providing more active sites for photon absorption and charge separation. A higher density of Fe₃O₄-ZnO-ZnS interfaces allows better spatial separation of e^-/h^+ pairs, delaying recombination and enhancing redox reactions. However, excessive loading may cause light scattering or shielding effects, which limit light penetration and reduce efficiency. Figure 8 demonstrates that near-neutral to slightly alkaline pH (7-9) supports optimal degradation performance. At pH 8, the surface charge of the nanocomposite and the ionization state of the pollutants favor adsorption. Additionally, alkaline conditions stabilize photogenerated holes (h^+) and increase the availability of hydroxyl ions (OH^-), which are essential for generating $^•OH$ radicals. At very low or high pH, excessive protonation or deprotonation can either neutralize h^+ or alter surface charge dynamics, promoting recombination.

4. MACHINE LEARNING PREDICTIVE ALGORITHMS

In this study, we introduce machine learning predictive algorithms to enhance our understanding of pollutant removal and concentration dynamics using the Fe_3O_4@BNPs@ZnO-ZnS nanocomposite. The chosen algorithms include Artificial Neural Networks (ANN), Random Forest (RF), and Support Vector Regression (SVR) [46-48].

ANNs consist of interconnected neurons that are organized into layers [49]. ANN models are very capable and able to predict intricate physical relations [50]. RF is an ensemble learning method that combines multiple decision trees to improve predictive accuracy [51]. The main advantage of RF is its ability to avoid overfitting in both classification and regression [52]. SVR is a powerful regression technique that finds the optimal hyperplane to minimize prediction errors, and it is very adept at processing non-linear relations [53].

In order to achieve the highest accuracy in all the ML models, hyperparameter tuning is required. This process involves optimizing the settings of the algorithms [54]. We will employ grid search [55] to adjust these parameters in each of the algorithms. Grid search uses a range of hyperparameter values and evaluates the model's performance with each combination. The most significant parameters in ANN include the number of hidden layers, the number of neurons in each layer, the activation functions, and the learning rate. For the RF model, optimizing parameters are the number of decision trees (n_estimators), maximum depth of trees (max_depth), and minimum samples required to split a node (min_samples_split). Finally, for SVR, hyperparameter tuning will focus on parameters like the kernel type, regularization parameter (C), and kernel coefficient (gamma).

Furthermore, an input selection procedure has been done for our study. Input parameters with the highest effect on the output are evaluated by a Pearson Correlation heatmap, which is depicted in Figure 10. In our study, we assessed the correlations among time, C_0 (initial pollutant concentration), pH, and UV (UV radiation intensity).
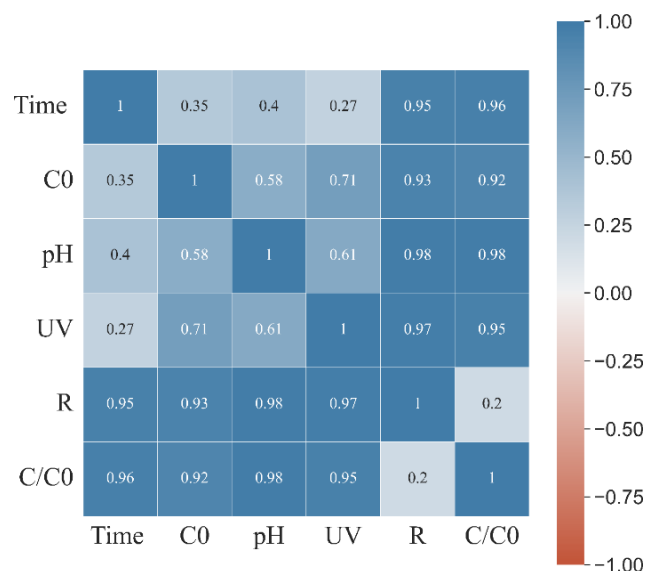

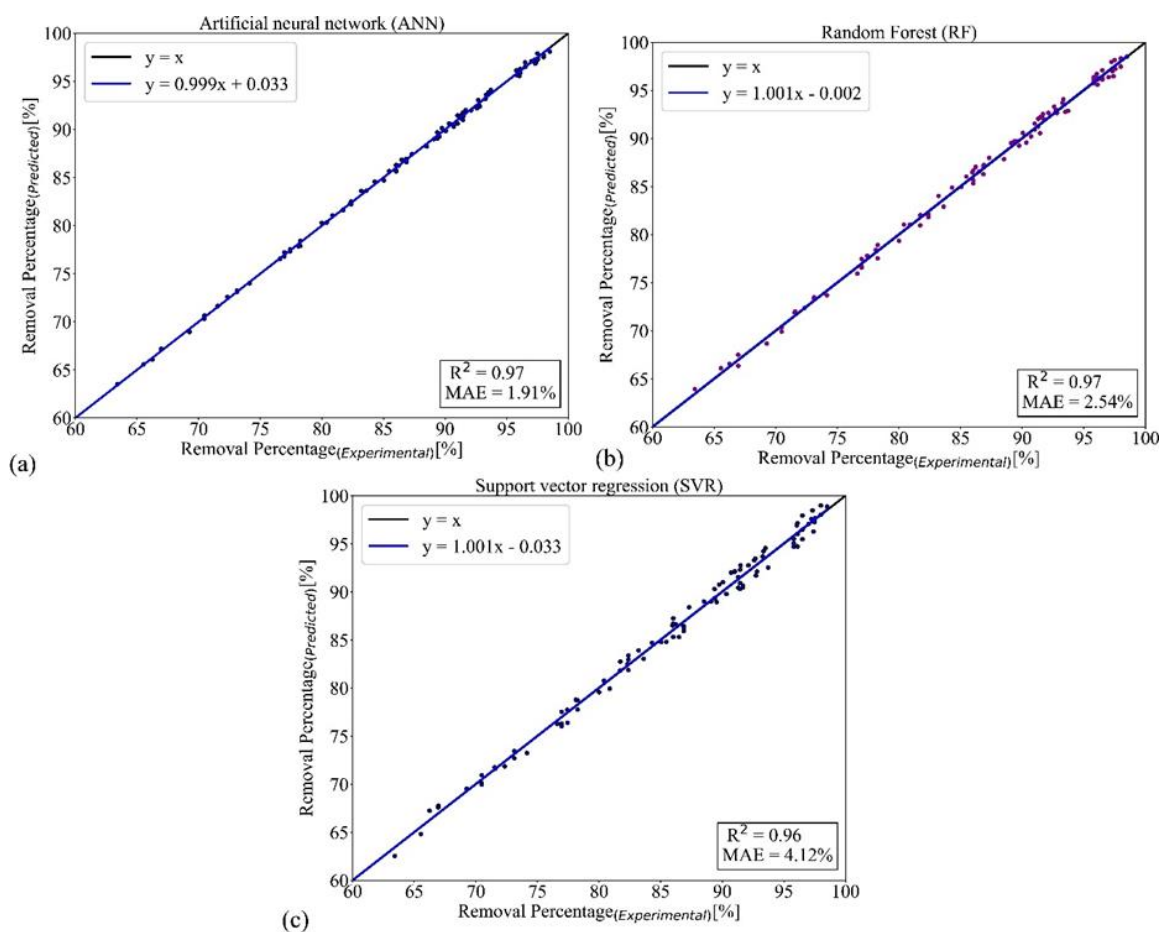**Figure 10.** The feature selection procedure for R and C/C_0

Figure 11. The predictive results of removal percentage by (a) ANN, (b) RF, and (c) SVR
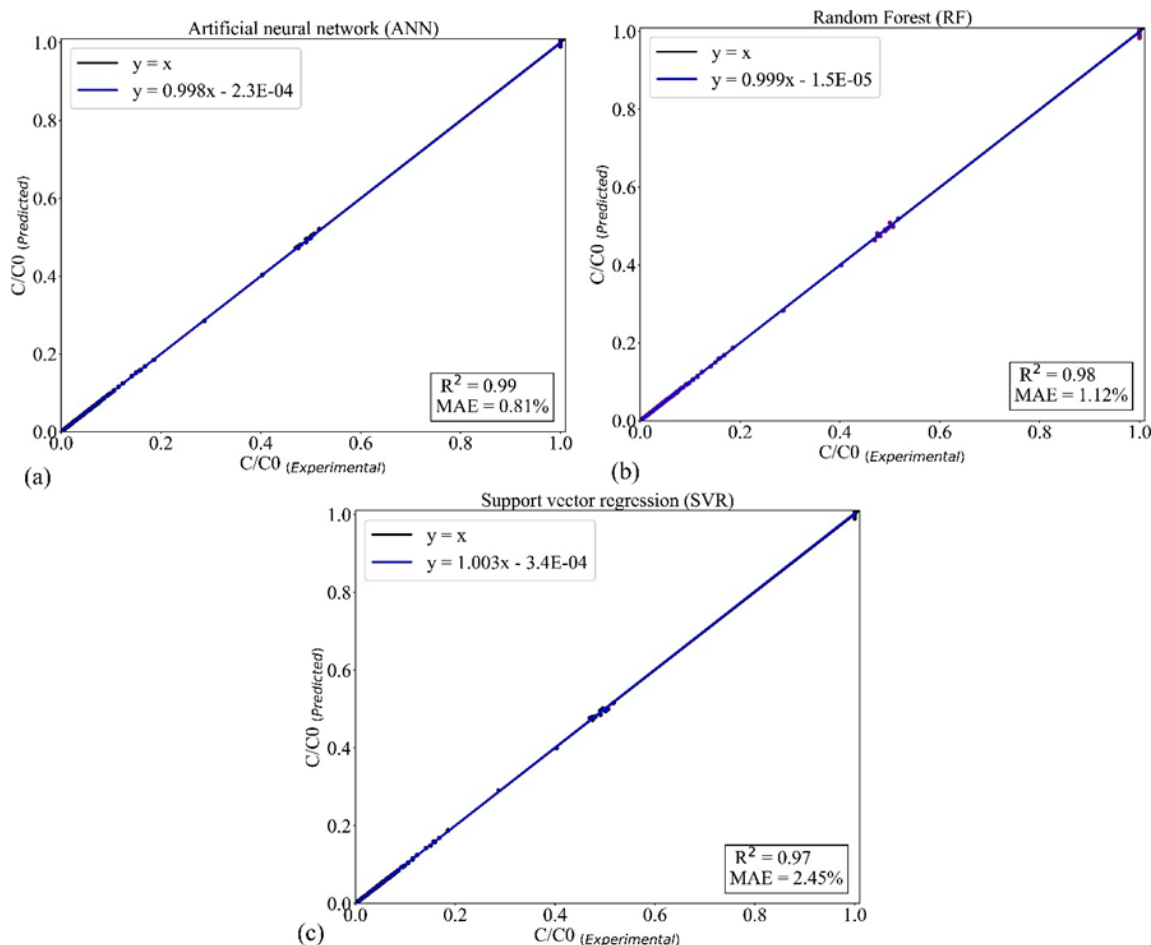
Figure 12. The predictive results of C/C_0 by (a) ANN, (b) RF, and (c) SVR

4.1 Predictive performance

After hyperparameter tuning, we will compare the predictive performance of the tuned ANN, RF, and SVR models for both pollutant removal and concentration ratios (C/C_0). We used the experimental dataset that we derived from our own experiments (120 data points) to train and test the models. A ratio of 70/30% has been used to, respectively, train and test the models.

The results of predictive models for the removal percentage of all three materials are presented in Figure 11. The ANN model had three hidden layers with 100 neurons. The Rectified Linear Unit (ReLU) activation function was employed, and the learning rate was 0.001. The batch size was 32, and the model underwent 10,000 epochs of training. The model proved to be very accurate with an MAE of 1.97% and an R-squared Value (R^2) of 0.97. The RF algorithm had a total of 100 decision trees, and the maximum depth of each tree was limited to 10 levels to prevent overfitting. A minimum requirement of 2 samples per leaf node was imposed. This model had an MAE of approximately 2.54% and an R-squared value of 0.97. The SVR model employed the Radial Basis Function (RBF) kernel, which is known for its ability to capture complex patterns in the data [53]. The regularization parameter (C) was 10 to balance the trade-off between achieving a low training error and maintaining model generalization. Furthermore, epsilon was set to 0.1 to allow some degree of flexibility in predictions. The accuracy of this model was an MAE of 4.12 and an R^2 of 0.96.

Also, the predictive models for C/C_0 are presented in Figure

12. The settings for the ANN model are also similar to those of the removal model, and the accuracy is an MAE of 0.81% and an R^2 of 0.99. The RF and SVR showed MAE of 1.12% and 2.45% respectively. Therefore, the most accurate model for C/C_0 is RF.

5. CONCLUSION

The Fe$_3$O$_4$@BNPs@ZnO-ZnS nanocomposite exhibits strong potential for advanced photocatalytic water treatment, supported by both experimental performance and predictive modeling. The key findings of this study are summarized as follows:

- Successful synthesis of a magnetically recoverable Fe$_3$O$_4$@BNPs@ZnO-ZnS nanocomposite.
- XRD and FTIR analyses confirm structural integrity and synergistic bandgap tuning (Fe$_3$O$_4$: 0.1 eV; ZnO: 3.37 eV).
- Photoluminescence measurements indicate enhanced charge carrier lifetime (8.7 ns vs. 2.1 ns in bare ZnO).
- Achieves 95-99.7% pollutant removal under optimized conditions (UV = 10 W, pH = 8, catalyst loading = 3 g/L).
- Magnetic recovery enables reuse with <1% catalyst loss per cycle.
- ANN, RF, and SVR models demonstrate excellent predictive accuracy with $R^2 \geq 0.96$ and low MAE for both pollutant removal and concentration ratios.
- Models were tuned via grid search and evaluated across three distinct pollutants, confirming generalization

potential.

To advance this platform, we plan to evaluate long-term catalyst stability under real wastewater conditions and expand ML training to model emerging contaminants such as PFAS and pharmaceutical residues.

REFERENCES

[1] Xiang, W., Zhang, X., Chen, J., Zou, W., He, F., Hu, X., Tsang, D.C., Ok, Y.S., Gao, B. (2020). Biochar technology in wastewater treatment: A critical review. Chemosphere, 252: 126539. https://doi.org/10.1016/j.chemosphere.2020.126539

[2] Mahmood, H., Hassan, M.S., Meraj, G., Furqan, M. (2024). Agriculture's role in environmental sustainability: A comprehensive review of challenges and solutions. Challenges in Sustainability, 12(3): 178-189. https://doi.org/10.56578/cis120302

[3] El Jery, A., Kosarirad, H., Taheri, N., Bagheri, M., Aldrdery, M., Elkhaleefa, A., Wang, C., Sammen, S.S. (2023). An application of ultrasonic waves in the pretreatment of biological sludge in urban sewage and proposing an artificial neural network predictive model of concentration. Sustainability, 15(17): 12875. https://doi.org/10.3390/su151712875

[4] Alimoradi, H., Shams, M. (2017). Optimization of subcooled flow boiling in a vertical pipe by using artificial neural network and multi objective genetic algorithm. Applied Thermal Engineering, 111: 1039-1051.
https://doi.org/10.1016/j.applthermaleng.2016.09.114

[5] El Jery, A., Aldrdery, M., Shirode, U.R., Gavilán, J.C.O., Elkhaleefa, A., Sillanpää, M., Sammen, S.S., Tizkam, H.H. (2023). An efficient investigation and machine learning-based prediction of decolorization of wastewater by using zeolite catalyst in electro-Fenton reaction. Catalysts, 13(7): 1085. https://doi.org/10.3390/catal13071085

[6] Fernández, L., Gamallo, M., González-Gómez, M.A., Vázquez-Vázquez, C., Rivas, J., Pintado, M., Moreira, M.T. (2019). Insight into antibiotics removal: Exploring the photocatalytic performance of a Fe_3O_4/ZnO nanocomposite in a novel magnetic sequential batch reactor. Journal of Environmental Management, 237: 595-608. https://doi.org/10.1016/j.jenvman.2019.02.089

[7] Aragaw, T.A., Bogale, F.M., Aragaw, B.A. (2021). Iron-based nanoparticles in wastewater treatment: A review on synthesis methods, applications, and removal mechanisms. Journal of Saudi Chemical Society, 25(8): 101280. https://doi.org/10.1016/j.jscs.2021.101280

[8] Merchán-Sanmartín, B., Álava-Zúñiga, B., Vallejo-Palomeque, F., Suárez-Zamora, S., Aguilar-Aguilar, M., Morante-Carballo, F. (2025). Integrated wastewater management for environmental protection and sustainable ecotourism in an Andean Paramo Community. Challenges in Sustainability, 13(3): 334-353. https://doi.org/10.56578/cis130302

[9] Xu, Z., Bai, X., Ye, Z. (2021). Removal and generation of microplastics in wastewater treatment plants: A review. Journal of Cleaner Production, 291: 125982. https://doi.org/10.1016/j.jclepro.2021.125982

[10] Ziajahromi, S., Neale, P.A., Silveira, I.T., Chua, A., Leusch, F.D. (2021). An audit of microplastic abundance throughout three Australian wastewater treatment plants. Chemosphere, 263: 128294. https://doi.org/10.1016/j.chemosphere.2020.128294

[11] Samawi, K.A., Salman, E.A.A., Alshekhly, B.A.A., Nassar, M.F., Borzehandani, M.Y., Abdulkareem-Alsultan, G., Latif, M.A.M., Abdulmalek, E. (2022). Rational design of different π-bridges and their theoretical impact on indolo [3, 2, 1-*jk*] carbazole based dye-sensitized solar cells. Computational and Theoretical Chemistry, 1212: 113725. https://doi.org/10.1016/j.comptc.2022.113725

[12] Idan, M.H., Kadhim, R.G., Mohammed, M.A. (2023). Preparation and study of the effect of adding cobalt and magnesium on the morphological, optical properties and bacterial activity of cadmium sulfide compound. AIP Conference Proceedings, 2977: 040117. https://doi.org/10.1063/5.0181726

[13] Chen, H., Tu, Z., Wu, S., Yu, G., Du, C., Wang, H., Yang, E., Zhou, L., Deng, B., Wang, D., Li, H. (2021). Recent advances in partial denitrification-anaerobic ammonium oxidation process for mainstream municipal wastewater treatment. Chemosphere, 278: 130436. https://doi.org/10.1016/j.chemosphere.2021.130436

[14] Afiqah-Idrus, A., Abdulkareem-Alsultan, G., Asikin-Mijan, N., Nassar, M.F., Voon, L., Teo, S.H., Kurniawan, T.A., Adzahar, N.A., Surahim, M., Razali, S.Z., Islam, A. (2024). Deoxygenation of waste sludge palm oil into hydrocarbon rich fuel over carbon-supported bimetallic tungsten-lanthanum catalyst. Energy Conversion and Management: X, 23: 100589. https://doi.org/10.1016/j.ecmx.2024.100589

[15] Tang, N., Liu, X., Xing, W. (2020). Microplastics in wastewater treatment plants of Wuhan, Central China: Abundance, removal, and potential source in household wastewater. Science of the Total Environment, 745: 141026. https://doi.org/10.1016/j.scitotenv.2020.141026

[16] Goutham, R., Rohit, P., Vigneshwar, S.S., Swetha, A., Arun, J., Gopinath, K.P., Pugazhendhi, A. (2022). Ionic liquids in wastewater treatment: A review on pollutant removal and degradation, recovery of ionic liquids, economics and future perspectives. Journal of Molecular Liquids, 349: 118150. https://doi.org/10.1016/j.molliq.2021.118150

[17] Ortega-Quispe, K., Ccopi-Trucios, D., Lozano-Povis, A., Llanos-del-Pino, A., Gabriel-Campos, E., Cordova-Buiza, F. (2024). Sustainable management of wastewater sludge through composting with effective microorganisms: Enhancing the growth of Tecoma stans. Organic Farming, 10(2): 108-119. https://doi.org/10.56578/of100202

[18] Masiá, P., Sol, D., Ardura, A., Laca, A., Borrell, Y.J., Dopico, E., Laca, A., Machado-Schiaffino, G., Díaz, M., Garcia-Vazquez, E. (2020). Bioremediation as a promising strategy for microplastics removal in wastewater treatment plants. Marine Pollution Bulletin, 156: 111252. https://doi.org/10.1016/j.marpolbul.2020.111252

[19] Mohammed, M.A. (2025). The effect of substrate temperature on the nanostructured V_2O_5 thin films, studying their structural, optical properties and testing as gas sensors. Journal of Nanostructures, 15(1): 200-209. https://doi.org/10.22052/JNS.2025.01.019

[20] Jassim, N.M., Ibrahim, N.I., Khalaf, N.Z. (2024). Z-scan study of the non-linear optical properties of

silver/curcumin dye nanocomposites prepared via nanosecond pulsed laser ablation. Revue des Composites et des Matériaux Avancés-Journal of Composite and Advanced Materials, 34(4): 533-540. https://doi.org/10.18280/rcma.340415

[21] Alshaeer, F., Mohammed, M.A., Zorah, M., Alharbi, N., Mahmoud, H.M.A., Ahmed, A.M.E., Mohammed, B.A., Abdulkareem-AlSultan, G., Nassar, M.F. (2025). Synergistic defect passivation and charge transport enhancement via thiosemicarbazide-functionalized carbon nanotubes for high-efficiency lead-free $CsSnI_3$ perovskite solar cells: A pathway to 23.34% efficiency. Journal of Alloys and Compounds, 1026: 180428. https://doi.org/10.1016/j.jallcom.2025.180428

[22] He, L., Lv, L., Pillai, S.C., Wang, H., Xue, J., Ma, Y., Liu, Y., Chen, Y., Wu, L., Zhang, Z., Yang, L. (2021). Efficient degradation of diclofenac sodium by periodate activation using Fe/Cu bimetallic modified sewage sludge biochar/UV system. Science of the Total Environment, 783: 146974. https://doi.org/10.1016/j.scitotenv.2021.146974

[23] Gholipour, A., Zahabi, H., Stefanakis, A.I. (2020). A novel pilot and full-scale constructed wetland study for glass industry wastewater treatment. Chemosphere, 247: 125966. https://doi.org/10.1016/j.chemosphere.2020.125966

[24] Jassim, N.M. (2024). Synthesis and nonlinear optical responses of Ag: ZnO core: Shell nanoparticles induced by Z-scan technique. Journal of Optics, 6: 02432. https://doi.org/10.1007/s12596-024-02432-6

[25] Hou, J., Chen, Z., Gao, J., Xie, Y., Li, L., Qin, S., Wang, Q., Mao, D., Luo, Y. (2019). Simultaneous removal of antibiotics and antibiotic resistance genes from pharmaceutical wastewater using the combinations of up-flow anaerobic sludge bed, anoxic-oxic tank, and advanced oxidation technologies. Water Research, 159: 511-520. https://doi.org/10.1016/j.watres.2019.05.034

[26] Chu, L., Wang, J., He, S., Chen, C., Wojnárovits, L., Takács, E. (2021). Treatment of pharmaceutical wastewater by ionizing radiation: Removal of antibiotics, antimicrobial resistance genes and antimicrobial activity. Journal of Hazardous Materials, 415: 125724. https://doi.org/10.1016/j.jhazmat.2021.125724

[27] Jassim, N.M., Wang, K., Han, X., Long, H., Wang, B., Lu, P. (2017). Plasmon assisted enhanced second-harmonic generation in single hybrid Au/ZnS nanowires. Optical Materials, 64: 257-261. https://doi.org/10.1016/j.optmat.2016.11.034

[28] Duan, X., Zhou, X., Wang, R., Wang, S., Ren, N.Q., Ho, S.H. (2021). Advanced oxidation processes for water disinfection: Features, mechanisms and prospects. Chemical Engineering Journal, 409: 128207. https://doi.org/10.1016/j.cej.2020.128207

[29] Guo, K., Wu, Z., Chen, C., Fang, J. (2022). UV/chlorine process: An efficient advanced oxidation process with multiple radicals and functions in water treatment. Accounts of Chemical Research, 55(3): 286-297. https://doi.org/10.1021/acs.accounts.1c00269

[30] El Jery, A., Salman, H.M., Al-Khafaji, R.M., Nassar, M.F., Sillanpää, M. (2023). Thermodynamics investigation and artificial neural network prediction of energy, exergy, and hydrogen production from a solar thermochemical plant using a polymer membrane electrolyzer. Molecules, 28(6): 2649.

https://doi.org/10.3390/molecules28062649

[31] Dizayee, W., Hamarashid, M.M., Zorah, M., Mahmoud, H.M., Al-Bahrani, M., Taki, A.G., Abdulkareem-Alsultan, G., Nassar, M.F. (2024). Synergistic effect of $Ni(OH)_2$ and MXene nanosheets in 3D framework on the improvement of dielectric, energy storage, mechanical and thermal characteristics of polyvinylidene fluoride (PVDF) polymeric composites. Journal of Alloys and Compounds, 1004: 175825. https://doi.org/10.1016/j.jallcom.2024.175825

[32] Samawi, K.A., Mohammed, B.A., Salman, E.A.A., Mahmoud, H.M., Sameen, A.Z., Mohealdeen, S.M., Abdulkareem-Alsultan, G., Nassar, M.F. (2024). Vertical growth of a 3D Ni–Co-LDH/N-doped graphene aerogel: A cost-effective and high-performance sulfur host for Li–S batteries. Physical Chemistry Chemical Physics, 26(12): 9284-9294. https://doi.org/10.1039/D3CP05716J

[33] Taoufik, N., Boumya, W., Achak, M., Sillanpää, M., Barka, N. (2021). Comparative overview of advanced oxidation processes and biological approaches for the removal pharmaceuticals. Journal of Environmental Management, 288: 112404. https://doi.org/10.1016/j.jenvman.2021.112404

[34] Ma, S., Zhan, S., Jia, Y., Zhou, Q. (2015). Superior antibacterial activity of Fe_3O_4-TiO_2 nanosheets under solar light. ACS Applied Materials & Interfaces, 7(39): 21875-21883. https://doi.org/10.1021/acsami.5b06264

[35] Zhang, Z., Fang, Y., Zhuo, L., Yuan, H., Zhang, L. (2022). Reduced graphene oxide wrapped Fe_3O_4@TiO_2 yolk–shell nanostructures as a magnetic recyclable photocatalytic antibacterial agent. Journal of Alloys and Compounds, 904: 164001. https://doi.org/10.1016/j.jallcom.2022.164001

[36] Alsultan, A.G., Asikin-Mijan, N., Obeas, L.K., Islam, A., Mansir, N., Teo, S.H., Razali, S.Z., Nassar, M.F., Mohamad, S., Taufiq-Yap, Y.H. (2022). Selective deoxygenation of sludge palm oil into diesel range fuel over Mn-Mo supported on activated carbon catalyst. Catalysts, 12(5): 566. https://doi.org/10.3390/catal12050566

[37] Sundui, B., Ramirez Calderon, O.A., Abdeldayem, O.M., Lázaro-Gil, J., Rene, E.R., Sambuu, U. (2021). Applications of machine learning algorithms for biological wastewater treatment: Updates and perspectives. Clean Technologies and Environmental Policy, 23(1): 127-143. https://doi.org/10.1007/s10098-020-01993-x

[38] Eskandari, E., Alimoradi, H., Pourbagian, M., Shams, M. (2024). Enhanced predictive modeling of Nusselt number in boiler tubes: Numerical simulations and machine learning for water and SiO_2/water. Journal of Thermal Analysis and Calorimetry, 149(17): 10119-10148. https://doi.org/10.1007/s10973-024-13409-9

[39] Talath, S., Wali, A.F., Sridhar, S.B., Hani, U., Alanazi, M., Alharby, T.N. (2024). Development of ions adsorption onto nanoparticles from water/wastewater sources via novel nanocomposite materials: A machine learning-based approach. Advanced Powder Technology, 35(6): 104462. https://doi.org/10.1016/j.apt.2024.104462

[40] Sharmila, V.G., Kumar, M.D., Tamilarasan, K. (2024). Machine learning-driven advances in metal-organic framework nanomaterials for wastewater treatment:

Developments and challenges. Separation & Purification Reviews, 1-21. https://doi.org/10.1080/15422119.2024.2437408

[41] Samawi, K.A., Salman, E.A.A., Hasan, H.A., Mahmoud, H.M., Mohealdeen, S.M., Abdulkareem-Alsultan, G., Abdulmalek, E., Nassar, M.F. (2024). Single-atom cobalt encapsulated in carbon nanotubes as an effective catalyst for enhancing sulfur conversion in lithium-sulfur batteries. Molecular Systems Design & Engineering, 9(5): 464-476. https://doi.org/10.1039/D3ME00191A

[42] Farrokhi, M., Hosseini, S.C., Yang, J.K., Shirzad-Siboni, M. (2014). Application of ZnO–Fe_3O_4 nanocomposite on the removal of azo dye from aqueous solutions: Kinetics and equilibrium studies. Water, Air, & Soil Pollution, 225: 1-12. https://doi.org/10.1007/s11270-014-2113-8

[43] Hassan, A., Samawi, K.A., Nassar, M.F., Haddad, R., Roostaie, A., Sadeghzadeh, S.M. (2023). Synthesis of cyclic carbonate from carbon dioxide and epoxides using bicobalt complexes absorbed on DFNS. Catalysis Letters, 153(10): 2900-2909. https://doi.org/10.1007/s10562-022-04130-z

[44] Mustafa, M.A., Abdullah, A.R., Hasan, W.K., Habeeb, L.J., Nassar, M.F. (2021). Two-way fluid-structure interaction study of twisted tape insert in a circular tube having integral fins with nanofluid. Eastern-European Journal of Enterprise Technologies, 3(8(111): 25-34. https://doi.org/10.15587/1729-4061.2021.234125

[45] Aslan, N. (2022). Synthesis and characterization of ZnO@Fe_3O_4 composite nanostructures by using hydrothermal synthesis method. Turkish Journal of Nature and Science, 11(1): 95-101. https://doi.org/10.46810/tdfd.1011220

[46] Alshaeer, F., Zorah, M., Mahmoud, H.M., Abdalgadir, L.M., Taki, A.G., Mohammed, B.A., Abdulkareem-Alsultan, G., Nassar, M.F. (2025). Bandgap-engineered MXene-g-C_3N_4 interfacial layer for enhanced charge carrier dynamics in perovskite solar cells. Journal of Alloys and Compounds, 1011: 178247. https://doi.org/10.1016/j.jallcom.2024.178247

[47] Yuldasheva, S., Fayzullaev, N., Khamdamova, S., Nazirova, R., Dilmurod, E., Mahmoud, H.M., Nassar, M.F. (2024). Enhanced tetracycline degradation in pharmaceutical wastewater via S-scheme photocatalysis using graphydine quantum dots/Janus MoSSe heterostructures. Journal of Water Process Engineering, 68: 106470. https://doi.org/10.1016/j.jwpe.2024.106470

[48] Alharbi, N., Alotaibi, M.M., Obeas, L.K., Marhoon, I.I., Zorah, M., Taki, A.G., Mohammed, B.A., Abdulkareem-Alsultan, G., Nassar, M.F. (2025). Boosting efficiency and long-lifespan in perovskite solar cells via 2D-MXene/Janus MoSSe integration. Journal of Alloys and Compounds, 1013: 178501. https://doi.org/10.1016/j.jallcom.2025.178501

[49] Rahman, R.A., Moamen, O.A., Abdelmonem, N., Ismail, I.M. (2019). Optimizing the removal of strontium and cesium ions from binary solutions on magnetic nano-zeolite using response surface methodology (RSM) and artificial neural network (ANN). Environmental Research, 173: 397-410. https://doi.org/10.1016/j.envres.2019.03.055

[50] Baştürk, E., Alver, A. (2019). Modeling azo dye removal by sono-Fenton processes using response surface methodology and artificial neural network approaches. Journal of Environmental Management, 248: 109300. https://doi.org/10.1016/j.jenvman.2019.109300

[51] Zamani Joharestani, M., Cao, C., Ni, X., Bashir, B., Talebiesfandarani, S. (2019). $PM_{2.5}$ prediction based on random forest, XGBoost, and deep learning using multisource remote sensing data. Atmosphere, 10(7): 373. https://doi.org/10.3390/atmos10070373

[52] Zhou, P., Li, Z., Snowling, S., Baetz, B.W., Na, D., Boyd, G. (2019). A random forest model for inflow prediction at wastewater treatment plants. Stochastic Environmental Research and Risk Assessment, 33: 1781-1792. https://doi.org/10.1007/s00477-019-01732-9

[53] Jana, D.K., Bhunia, P., Adhikary, S.D., Bej, B. (2022). Optimization of effluents using artificial neural network and support vector regression in detergent industrial wastewater treatment. Cleaner Chemical Engineering, 3: 100039. https://doi.org/10.1016/j.clce.2022.100039

[54] Eskandari, E., Alimoradi, H., Pourbagian, M., Shams, M. (2022). Numerical investigation and deep learning-based prediction of heat transfer characteristics and bubble dynamics of subcooled flow boiling in a vertical tube. Korean Journal of Chemical Engineering, 39(12): 3227-3245. https://doi.org/10.1007/s11814-022-1267-0

[55] Kovacs, D.J., Li, Z., Baetz, B.W., Hong, Y., Donnaz, S., Zhao, X., Zhou, P., Ding, H., Dong, Q. (2022). Membrane fouling prediction and uncertainty analysis using machine learning: A wastewater treatment plant case study. Journal of Membrane Science, 660: 120817. https://doi.org/10.1016/j.memsci.2022.120817

NOMENCLATURE

ANN	Artificial Neural Network
BNPS	Boehmite nanoparticles
C	Pollutant concentration, mg·L^{-1}
C_0	Initial pollutant concentration, mg·L^{-1}
C/C_0	Dimensionless concentration ratio
EDS	Energy Dispersive X-ray Spectroscopy
FESEM	Field-Emission Scanning Electron Microscopy
FTIR	Fourier Transform Infrared Spectroscopy
MAE	Mean Absolute Error
ML	Machine Learning
pH	Acidity/basicity level (dimensionless)
RF	Random Forest
R^2	Coefficient of determination (dimensionless)
SVR	Support Vector Regression
T	Time, min
UV	Ultraviolet radiation intensity, W
XRD	X-ray Diffraction